Motion compensation algorithm for online digital elevation map generation using scanning LIDAR data

Kari C. Ward*, Kyle W. Smith†
The Charles Stark Draper Laboratory

Gavin F. Mendeck‡
NASA Johnson Space Center

Renewed interest in lunar and eventually Martian surface exploration and science has resulted in increased demand for precision landing capabilities to safely deliver vehicles as close as possible to the desired target landing site. A recent technology under development to facilitate safe precision landing, the NASA Goddard Space Flight Center's hazard detection LIDAR (HDL), is designed to provide online digital elevation maps (DEMs) of the local terrain, without a requisite vehicle hover to perform the scan. The HDL produces a DEM in the presence of motion by applying a motion compensation algorithm developed by the Safe and Precision Landing Integrated Capabilities Evolution (SPLICE) navigation team. The algorithm is tailored to meet the strenuous requirements necessary to produce a real-time DEM by balancing computational complexity and accuracy. This paper details the algorithm for motion compensation, assumptions and simplifications necessary to deploy it on the HDL field programmable gate array (FPGA), sensitivities of the output point cloud to the aforementioned modifications, and results from HDL helicopter flight testing.

I. Introduction

Lunar surface exploration and science continues to be a primary goal of NASA through the Artemis [1] and Commercial Lunar Payload Services [2] programs. The problem of landing at hazardous locations in poor or no lighting conditions on the moon is not solved, and developments in hardware and software continue to advance the capabilities of such systems. The Safe and Precise Landing–Integrated Capability Evolution (SPLICE) project contributes to that effort to advance entry, descent, and landing (EDL) technologies. SPLICE builds upon the research and developments of Autonomous Landing and Hazard Avoidance Technologies (ALHAT) and Morpheus. Since the Morpheus test flights, more advancements have been made in developing hazard detection (HD)-related algorithms [3] and maturation of hazard scanning and safe site selection systems leveraging linear scanning LIDAR [4].

Similar to testing completed with ALHAT and Morpheus projects [5], the SPLICE focus has been on maturation of technologies for online digital elevation map (DEM) creation and safe site selection facilitated by the NASA Goddard hazard detection LIDAR (HDL) [6]. This mapping LIDAR points the beam by precise relative rotation between two spinning risley prisms, which allows programmable scan patterns. The original concept of operations for this cooperative SPLICE hazard detection, safe site selection, guidance and navigation framework begins with an HDL scan of the terrain surrounding the originally intended landing site at around 500m slant range. The point cloud from the scan is used to create a DEM that is fed to hazard detection and site selection algorithms. Once the safe site is selected, guidance and navigation perform a divert and new site estimation [7–9]. More details on this concept of operations can be found in Ref. [10].

The intermediary component necessary to turn the real time point cloud data into something that can be used to create a DEM is to correct for the motion of the sensor with respect to the surface from the start of the scan to the time of the range measurement. This process is referred to as motion correction, deskewing [11], or in this work, motion compensation. The motion compensation algorithm that follows was originally designed for hazard scanning and divert site selection in a lunar south pole landing concept of operations; the algorithm is not changed for terrestrial testing.

This paper is organized as follows. First, the helicopter testing details are discussed. Next, an overview of the motion compensation and state propagation process is presented. Details on the simplifications and assumptions required of the

*Senior Member of the Technical Staff
†Principal Member of the Technical Staff
‡SPLICE Project Manager

algorithm for flight testing are provided followed by a quantitative analysis of the effects of those simplifications. Finally a high level examination of the effects of simplified motion compensation on the moon, Mars, and Titan is provided, finishing with conclusions and future work.

A. Acronyms

ALHAT Autonomous Landing and Hazard Avoidance Technologies
CG center of gravity
DEM digital elevation map
ECI Earth-centered inertial
EDL entry, descent, and landing
ENU east-north-up
FPGA field programmable gate array
HDL hazard detection LIDAR
HD hazard detection
IMU inertial measurement unit
KSC Kennedy Space Center
LLA latitude, longitude, altitude
LVLH local vertical local horizontal
PCPF planet-centered planet-fixed
PVA position, velocity, and attitude
RSS root-sum-squared
SPLICE Safe and Precise Landing–Integrated Capability Evolution

II. Helicopter Testing

The NASA Goddard HDL was tested over several days in March 2025. This test campaign consisted of a series of helicopter flights at the Shuttle landing facility at Kennedy Space Center (KSC). Figure (1) depict the hazard field at the end of the runway. The HDL was hard mounted on the helicopter and the pilot manually adjusted the vehicle attitude so to point the sensor at the hazard field. For each flight, multiple scans were performed with the helicopter in a hover or on a glide slope descent with the HDL boresight pointed at the center of the hazard field. More details on the hazard detection findings from this test campaign can be found in Ref. [12].

For each scan, the HDL sensor fires and collects laser returns in a radial pattern, starting from the outer circumference and spiraling in towards the center. This results in more than a million range returns over the course of a two second scan. The range information, combined with precise knowledge of the sensor pointing direction in the sensor reference frame at that time, provides a range vector from the sensor to a surface intersection point. In order to bin and average the range vectors to produce a DEM, the surface intersections relative to the vehicle must be related via a common reference frame and time. The common reference frame, referred to as the DEM frame here, is defined by the local vertical local horizontal (LVLH) frame at time 0, the start of the scan. The corresponding DEM frame origin is defined by a predetermined distance along the HDL boresight at that time. The process by which the set of range vectors and corresponding intersection point information collected over the scan are related in the DEM frame is referred to here as motion compensation. This process accounts for the surface and sensor motion from time 0 to the time of a given range return. The resulting set of vectors from the sensor to the surface intersections, expressed in the DEM frame at time 0 is called the point cloud in this analysis.

III. Motion Compensation

Motion compensation is used to relate each of the laser intersection points, taken over the duration of the scan, to a common time, origin, and reference frame. For this problem, the time, origin, and reference frame are defined by the sensor LVLH at the start of the scan (time 0), with origin a predefined length along the boresight. The HDL sensor reference frame is defined with z-axis along the boresight, and x/y-axes arbitrarily selected such that a right-handed orthogonal reference frame is defined. This frame is assumed to have a known transformation to the inertial measurement unit (IMU) reference frame. The geometry of the problem is depicted in Figure (2), where the position of the laser intersection point p on the surface is related back to the position of the sensor s at the start of the scan.

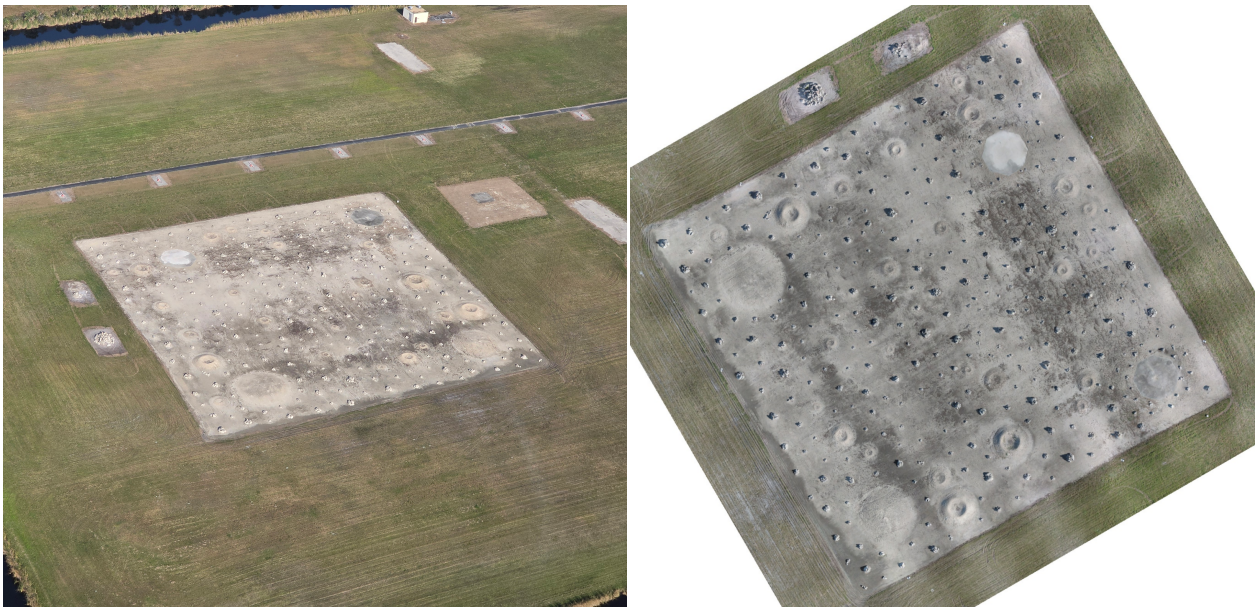

Fig. 1 KSC Shuttle landing facility hazard field, isometric (a) and top-down (b) views.

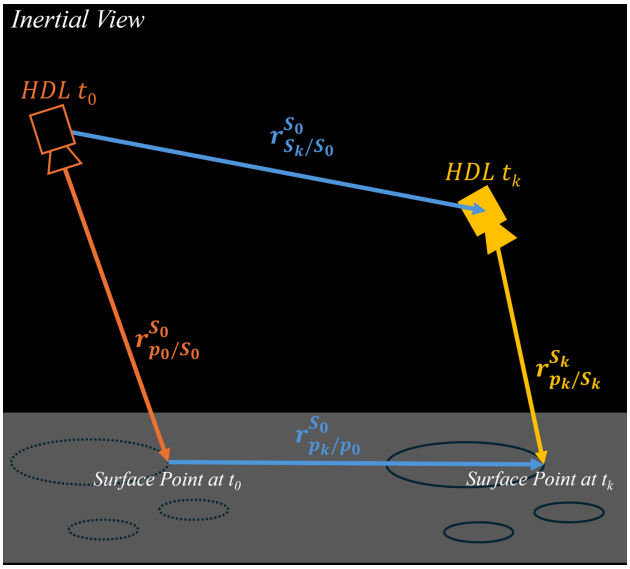

Fig. 2 Geometry of the motion compensation problem, where the change in position and orientation of the sensor and the surface at any given time must be related back to the scan time 0 (t_0). Surface features at t_0 are shown with dashed lines and at some future time k (t_k) with solid lines. Measurements taken at t_k are transformed into the sensor frame at time t_0.

The position $\boldsymbol{r}^{s_0}_{p_0/s_0}$ of the laser surface intersection point at time 0 with respect to the position of the sensor at time 0, expressed in the sensor reference frame at time 0 is defined as

$$\boldsymbol{r}^{s_0}_{p_0/s_0} = \boldsymbol{r}^{s_0}_{s_k/s_0} + \boldsymbol{T}^{s_0}_{s_k}\boldsymbol{r}^{s_k}_{p_k/s_k} - \boldsymbol{r}^{s_0}_{p_k/p_0} \tag{1}$$

where $\boldsymbol{r}^{s_0}_{s_k/s_0}$ is the translational motion of the sensor from time 0 to time k ($k \geq 0$), expressed in the sensor reference frame at time 0, $\boldsymbol{T}^{s_0}_{s_k}$ is the change in attitude of the sensor from time k to time 0, $\boldsymbol{r}^{s_k}_{p_k/s_k}$ is the surface intersection point relative to the sensor at time k (i.e. the sensor's range measurement along its pointing direction) expressed in the sensor

frame at time k, and $\boldsymbol{r}^{s_0}_{p_k/p_0}$ is the translational motion of the intersection point from time 0 to time k. Recognizing that the motion of a surface point is governed by the rotation of the primary body, the final term in Eq. (1) can be decomposed into

$$\boldsymbol{r}^{s_0}_{p_k/p_0} = \boldsymbol{T}^{s_0}_{i} \left(\left[\boldsymbol{T}^{i}_{f_k} \boldsymbol{\omega}^{f}_{f/i} \times \right] \boldsymbol{r}^{i}_{p_k/i} \left(t_k - t_0 \right) \right) \tag{2}$$

where $\boldsymbol{T}^{i}_{f_k}$ denotes the transformation from the planet-centered planet-fixed (PCPF) at time k to the inertial (i) frame, $\boldsymbol{\omega}^{f}_{f/i}$ is the angular rotation of the PCPF frame (f) with respect to the inertial frame, $\boldsymbol{r}^{i}_{p_k/i}$ is the inertially referenced surface point position vector at time k, and t_k and t_0 denote times k and 0. Or, in terms of sensor position and the sensor range vector at time k,

$$\boldsymbol{r}^{s_0}_{p_k/p_0} = \boldsymbol{T}^{s_0}_{i} \left(\left[\boldsymbol{T}^{i}_{f_k} \boldsymbol{\omega}^{f}_{f/i} \times \right] \left(\boldsymbol{r}^{i}_{s_k/i} + \boldsymbol{T}^{i}_{s_k} \boldsymbol{r}^{s_k}_{p_k/s_k} \right) \left(t_k - t_0 \right) \right) . \tag{3}$$

Substituting Eq. (3) back into Eq. (1) yields

$$\boldsymbol{r}^{s_0}_{p_0/s_0} = \boldsymbol{r}^{s_0}_{s_k/s_0} + \boldsymbol{T}^{s_0}_{s_k} \boldsymbol{r}^{s_k}_{p_k/s_k} - \boldsymbol{T}^{s_0}_{i} \left(\left[\boldsymbol{T}^{i}_{f_k} \boldsymbol{\omega}^{f}_{f/i} \times \right] \left(\boldsymbol{r}^{i}_{s_k/i} + \boldsymbol{T}^{i}_{s_k} \boldsymbol{r}^{s_k}_{p_k/s_k} \right) \left(t_k - t_0 \right) \right) \tag{4}$$

The primary function of motion compensation is to then book keep the change in position $\boldsymbol{r}^{s_0}_{s_k/s_0}$ and attitude $\boldsymbol{T}^{s_0}_{s_k}$ over the course of a scan such that each range returned from the sensor $\boldsymbol{r}^{s_k}_{p_k/s_k}$ can be mapped back to the selected time 0 reference frame and origin using Eq. (4).

IV. State Propagation

Ideally, motion compensation would be initialized at time 0 using the best estimate of the sensor position, velocity, and attitude (PVA). With the SPLICE flight software in the loop, that means relating the sensor pose to the navigation filter states. Accumulation of translational and rotational motion relative to the surface is performed using a primary-body centered inertial reference frame. This choice was made to allow for eventual development of DEM error mapping back to the SPLICE navigation filter states; however, this development is future work. For more details on how the DEM is currently used in the SPLICE navigation filter, see Ref. [8]. To maintain consistent as possible state estimation between motion compensation and navigation states, the filter's state propagation equations can be leveraged to compute the sensor position and orientation at each valid range return time. The navigation filter propagates the estimated inertial IMU PVA states using dead-reckoning of the IMU measurements. The attitude of the HDL at an arbitrary point in time is related to the filter estimated IMU attitude by

$$\bar{\boldsymbol{q}}^{s_k}_{i} = \bar{\boldsymbol{q}}^{s}_{imu} \otimes \bar{\boldsymbol{q}}^{imu_k}_{i} \tag{5}$$

where $\bar{\boldsymbol{q}}^{s}_{imu}$ is the constant, assumed known, quaternion for the sensor frame orientation with respect to the IMU frame, and $\bar{\boldsymbol{q}}^{imu_k}_{i}$ is the quaternion for the transformation from the inertial to the IMU frame. The inertial position of the HDL at an arbitrary point in time is given by

$$\boldsymbol{r}^{i}_{s/i} = \boldsymbol{r}^{i}_{imu/i} + \boldsymbol{T}^{i}_{imu} \boldsymbol{r}^{imu}_{s/imu} , \tag{6}$$

where $\boldsymbol{T}^{i}_{imu}$ is the transformation associated with the inverse of the inertial to IMU quaternion in Eq. (5), $\boldsymbol{r}^{imu}_{s/imu}$ is the known position vector of the sensor with respect to the IMU, and $\boldsymbol{r}^{i}_{imu/i}$ is the filter's estimated inertial position of the IMU.

IMU measurements are provided as the measured (denoted $(\circ)_m$) non-gravitational acceleration $\left(\dot{\boldsymbol{v}}^{imu}_{imu/i} \right)_m$ and angular velocity $\left(\dot{\boldsymbol{\theta}}^{imu}_{imu/i} \right)_m$ of the sensor, along with the sample rate of the sensor Δt. The measured rates are assumed to be corrupted by biases of the accelerometer $\boldsymbol{b}^{imu}_{accel}$ and gyroscope $\boldsymbol{b}^{imu}_{gyro}$ that are estimated by the filter. Using these biases and the sensor sample rate, the compensated IMU change in velocity and attitude over the sample period are given by

$$\Delta \boldsymbol{v}^{imu}_{imu/i} = \left(\left(\dot{\boldsymbol{v}}^{imu}_{imu/i} \right)_m - \boldsymbol{b}^{imu}_{accel} \right) \Delta t \tag{7}$$

$$\Delta \boldsymbol{\theta}^{imu}_{imu/i} = \left(\left(\dot{\boldsymbol{\theta}}^{imu}_{imu/i} \right)_m - \boldsymbol{b}^{imu}_{gyro} \right) \Delta t \tag{8}$$

The inertial position $\boldsymbol{r}^i_{imu}$, velocity $\boldsymbol{v}^i_{imu}$, and attitude $\bar{\boldsymbol{q}}^{imu}_i$ estimates of the navigation filter must be propagated from time t_k to time $t_{k+1} = t_k + \Delta t$. Note here the subscript denoting the position and velocity are referenced to the inertial origin is omitted for brevity. The compensated IMU data relating the change in velocity and attitude from time step k to $k+1$, ($\Delta \boldsymbol{v}^{imu_k}_{imu_{k+1}/i}$, $\Delta \boldsymbol{\theta}^{imu_k}_{imu_{k+1}/i}$), are applied in the discrete propagation equations for position,

$$\begin{aligned}\boldsymbol{r}^i_{imu_{k+1}} = \boldsymbol{r}^i_{imu_k} &+ \boldsymbol{v}^i_{imu_k}\Delta t \\ &+ \frac{1}{2}\boldsymbol{T}^i_{imu_k}\left(\boldsymbol{I}_3 + \frac{1}{3}\left[\Delta\boldsymbol{\theta}^{imu_k}_{imu_{k+1}/i}\times\right]\right)\Delta\boldsymbol{v}^{imu_k}_{imu_{k+1}/i}\Delta t \\ &+ \frac{1}{2}\left(\boldsymbol{g}^i_{cg_k} - \frac{1}{3}\boldsymbol{G}_k\boldsymbol{T}^i_{imu_k}\left[\boldsymbol{r}^{imu}_{imu/cg}\times\right]\Delta\boldsymbol{\theta}^{imu_k}_{imu_{k+1}/i}\right)\Delta t^2\end{aligned} \tag{9}$$

velocity,

$$\begin{aligned}\boldsymbol{v}^i_{imu_{k+1}} = \boldsymbol{v}^i_{imu_k} &\\ &+ \boldsymbol{T}^i_{imu_k}\left(\boldsymbol{I}_3 + \frac{1}{2}\left[\Delta\boldsymbol{\theta}^{imu_k}_{imu_{k+1}/i}\times\right]\right)\Delta\boldsymbol{v}^{imu_k}_{imu_{k+1}/i} \\ &+ \left(\boldsymbol{g}^i_{cg_k} - \frac{1}{2}\boldsymbol{G}_k\boldsymbol{T}^i_{imu_k}\left[\boldsymbol{r}^{imu}_{imu/cg}\times\right]\Delta\boldsymbol{\theta}^{imu_k}_{imu_{k+1}/i}\right)\Delta t\end{aligned} \tag{10}$$

and attitude,

$$\bar{\boldsymbol{q}}^{imu_{k+1}}_i = \bar{\boldsymbol{q}}\left(\Delta\boldsymbol{\theta}^{imu_k}_{imu_{k+1}/i}\right)\otimes\bar{\boldsymbol{q}}^{imu_k}_i \tag{11}$$

where $\boldsymbol{T}^i_{imu_k}$ is the transformation matrix corresponding to the conjugate $\bar{\boldsymbol{q}}^{imu_k,-1}_i$ of the navigation attitude estimate, $\boldsymbol{g}^i_{cg_k}$ is the gravitational acceleration at the center of gravity (CG), $\boldsymbol{G}_k$ is the Jacobian corresponding to the gravitational model, $\boldsymbol{r}^{imu}_{imu/cg}$ is the lever arm from the CG to the IMU, and the "delta quaternion" for an arbitrary $\Delta\theta$ is defined as

$$\bar{\boldsymbol{q}}\left(\Delta\theta\right) = \begin{bmatrix}\sin\left(\frac{||\Delta\theta||}{2}\right)\frac{\Delta\theta}{||\Delta\theta||} \\ \cos\left(\frac{||\Delta\theta||}{2}\right)\end{bmatrix} \tag{12}$$

V. Implementation Requirements and Approach

To implement motion compensation online with the HDL on a test flight, the algorithm is designed to be as computationally light as possible while maintaining sufficient accuracy. The motivation for this trade-off is that the HDL produces on the order of 1-2 million returns over the course of a two second scan and the EDL concept of operations necessitates a system weight and DEM generation at a speed that do not allow for saving the raw range returns. Note, for helicopter flight testing these returns were captured for additional post-processing, such as this work. To ensure successful operation on the field programmable gate array (FPGA), the HDL team leveraged the following requirements on the motion compensation algorithm

- No navigation filter inputs after time 0 initialization
- No square roots
- No ephemeris or constants data stored on the FPGA

The first requirement for no navigation filter inputs during the scan means motion compensation must perform its own state propagation. However, the PVA propagation outlined in Eqs. (9)–(11) relies on square roots to compute several terms. For attitude propagation, this means the delta quaternion in Eq. (12) is not a valid parameterization of attitude in this context. Instead, the attitude is propagated using transformation matrices such that

$$\boldsymbol{T}^{imu_{k+1}}_i = \left(\boldsymbol{I}_3 - \left[\Delta\boldsymbol{\theta}^{imu_k}_{imu_{k+1}/i}\times\right]\right)\boldsymbol{T}^{imu_k}_i\,, \tag{13}$$

and the relationship in Eq. (5) can be similarly expressed via

$$\boldsymbol{T}^{s_k}_i = \boldsymbol{T}^s_{imu}\boldsymbol{T}^{imu_k}_i \tag{14}$$

With Eq. (13), the attitude can be propagated square-root free and without further assumptions for implementation. The change in sensor attitude over the scan $\boldsymbol{T}_{s_k}^{s_0}$ in Eq. (4) can then be incrementally computed with each new gyroscope measurement from

$$\boldsymbol{T}_{s_{k+1}}^{s_0} = \boldsymbol{T}_{s_k}^{s_0} \left(\boldsymbol{T}_{imu}^{s} \left(\boldsymbol{I}_3 + \left[\Delta\boldsymbol{\theta}_{imu_{k+1}/i}^{imu_k} \times \right] \right) \boldsymbol{T}_{s}^{imu} \right) \tag{15}$$

where $\boldsymbol{T}_{s_k}^{s_0}$ is initialized at $k = 0$ as an identity matrix.

While the attitude propagation is largely unaffected by the requirements, the position and velocity propagation in Eqs. (9) and (10) have several problematic components. Due to the requirements against storing constants or ephemeris data and square-roots, any type of gravity model would be in violation. To work around this constraint, the navigation filter is used to compute, and provide at time 0, a means for approximating the gravitational acceleration. Consider the spherical model for gravitational acceleration of the CG at time k,

$$\boldsymbol{g}_{cg_k}^{i} = -\frac{\mu \boldsymbol{r}_{cg_k}^{i}}{||\boldsymbol{r}_{cg_k}^{i}||^3} \tag{16}$$

where the position norm and constant μ are at odds with the requirements; the first, due to the square root necessary for the L2 norm, the latter because it would need to be stored in memory. Implicit in the gravity calculation in Eq. (16), or more specifically its implementation in Eqs. (9) and (10) is the need to either estimate or store the relative position of the CG with respect to the IMU. Instead of storing and/or computing these values online with motion compensation, an approximation

$$\tilde{g} = \frac{\mu}{||\boldsymbol{r}_{imu_0}^{i}||^3} \,, \tag{17}$$

is provided with the navigation state at time 0. The approximation in Eq. (17) adds the further assumption that the relative position of the CG with respect to the IMU is small enough to have negligible effect. Using this assumption and the approximation in Eq. (17), the gravitational acceleration of the IMU can be approximated at time k as

$$\boldsymbol{g}_{imu_k}^{i} \cong \boldsymbol{r}_{imu_k}^{i} \tilde{g} \,. \tag{18}$$

The gravitational model Jacobian $\boldsymbol{G}_k$ in Eqs. (9) and (10) also presents the same square-root issues that occur with the gravitational acceleration term. Since the $\boldsymbol{G}_k$ term in the propagation equations also depends on the relative position of the CG with respect to the IMU, applying the assumption that the offset is small enough to have negligible effect means the entire $\boldsymbol{G}_k$ term can be neglected.

The last simplification made to Eqs. (9) and (10) concerns the effect of rotational velocity in the propagation. Specifically the terms $\left(\boldsymbol{I}_3 + \frac{1}{3} \left[\Delta\boldsymbol{\theta}_{imu_{k+1}/i}^{imu_k} \times \right] \right)$ and $\left(\boldsymbol{I}_3 + \frac{1}{2} \left[\Delta\boldsymbol{\theta}_{imu_{k+1}/i}^{imu_k} \times \right] \right)$ for the position and velocity, respectively. Since the EDL concept of operations includes an attitude hold along the glide slope specifically for the HDL scan, effects of $\left[\Delta\boldsymbol{\theta}_{imu_{k+1}/i}^{imu_k} \times \right]$ are taken to be negligible as well. That is, the attitude and position/velocity propagation are decoupled.

Applying the simplifications for gravity modeling, CG offset effects, and angular rate effects in Eqs. (9) and (10) results in

$$\boldsymbol{r}_{imu_{k+1}}^{i} = \boldsymbol{r}_{imu_k}^{i} + \boldsymbol{v}_{imu_k}^{i} \Delta t + \frac{1}{2} \boldsymbol{T}_{imu_k}^{i} \Delta\boldsymbol{v}_{imu_{k+1}/i}^{imu_k} \Delta t + \frac{1}{2} \left(\boldsymbol{r}_{imu_k}^{i} \tilde{g} \right) \Delta t^2 \tag{19}$$

and

$$\boldsymbol{v}_{imu_{k+1}}^{i} = \boldsymbol{v}_{imu_k}^{i} + \boldsymbol{T}_{imu_k}^{i} \Delta\boldsymbol{v}_{imu_{k+1}/i}^{imu_k} + \left(\boldsymbol{r}_{imu_k}^{i} \tilde{g} \right) \Delta t \,, \tag{20}$$

respectively.

One final simplification in Eq. (2), and subsequently Eq. (4), is necessary to meet the motion compensation requirements. The fixed to inertial frame transformation at time k, $\boldsymbol{T}_{f_k}^{i}$, requires either a stored initial matrix at time 0 and propagation to time k or an onboard ephemeris, both of which violate the requirement against storing ephemeris or constants data on the FPGA. Similarly, the rotation rate of the fixed frame with respect to the inertial frame $\boldsymbol{\omega}_{f/i}^{f}$ would potentially need to be stored on the FPGA or sent with the filter states at time 0. Either way, the term requires an

approximation. Since the magnitude of this term should change very little over the course of a scan and is approximately the same for all surface points in the scan region, the decision was made to approximate the surface velocity term with a constant

$$\left[\boldsymbol{T}^{i}_{f_k}\boldsymbol{\omega}^{f}_{f/i}\times\right]\left(\boldsymbol{r}^{i}_{s_k/i}+\boldsymbol{T}^{i}_{s_k}\boldsymbol{r}^{s_k}_{p_k/s_k}\right)\cong\tilde{\boldsymbol{v}}=\left[\boldsymbol{T}^{i}_{f(0)}\boldsymbol{\omega}^{f}_{f/i}\times\right]\boldsymbol{r}^{i}_{s_0/i} \tag{21}$$

such that it can be computed by SPLICE navigation and sent along with the filter states at time 0. Incorporating this approximation in Eq. (4) results in

$$\boldsymbol{r}^{s_0}_{p_0/s_0}=\boldsymbol{r}^{s_0}_{s_k/s_0}+\boldsymbol{T}^{s_0}_{s_k}\boldsymbol{r}^{s_k}_{p_k/s_k}-\boldsymbol{T}^{s_0}_{i}\left(\tilde{\boldsymbol{v}}\left(t_k-t_0\right)\right) \tag{22}$$

To summarize, assumptions for the motion compensation are:

- Sensor rotation rate is low enough to adhere to the small angle assumption.
- Sensor rotation rate is low enough to not significantly contribute to the velocity.
- IMU biases can be taken as constant over the scan
- Inertial position magnitude changes, for the purposes of computing gravitational acceleration, are sufficiently small to be assumed constant.
- Effects due to the offset of the IMU and HDL from the vehicle CG are negligible
- Surface velocity vector is constant and identical for all range returns

A. HDL Motion Compensation

Motion compensation is initialized using the most recent SPLICE navigation filter data at time $t_k = t_0$. The cumulative change in position and attitude of the sensor are initialized as $\boldsymbol{r}^{s_0}_{s_k/s_0} = [0,\ 0,\ 0]^T$ and $\boldsymbol{T}^{s_0}_{s_k} = \boldsymbol{I}_3$. For each new range return from the HDL sensor $\boldsymbol{r}^{s_{k+1}}_{p_{k+1}/s_{k+1}}$, the position, velocity, and attitude of the IMU are propagated from the time of the previous range return at time t_k to the time of the new range at t_{k+1} via the most recent IMU rates. Additionally, the incremental change in position and attitude of the HDL are incorporated into the tracked changes since time 0. Algorithm 1 details this process.

The motion compensation algorithm corrects for IMU biases to mitigate the effects of those corruptions on the resulting point cloud. However, one of the largest error contributions in the motion compensation would be the misalignment of the HDL with respect to the IMU. That transformation, $\boldsymbol{T}^{s}_{imu}$, is assumed to be time-invariant and known in this analysis. Unfortunately, the helicopter testing and lunar EDL concepts of operation do not provide a means to estimate error in that transformation, therefore compensation for such a misalignment is omitted from the algorithm.

Algorithm 1: Motion Compensation for HDL

Main($\boldsymbol{r}^{i}_{imu_k}$, $\boldsymbol{v}^{i}_{imu_k}$, $\boldsymbol{T}^{imu_k}_{i}$, $\boldsymbol{b}^{imu}_{accel}$, $\boldsymbol{b}^{imu}_{gyro}$, $\left(\dot{\boldsymbol{v}}^{imu}_{imu/i}\right)_{m,k+1}$, $\left(\dot{\boldsymbol{\theta}}^{imu}_{imu/i}\right)_{m,k+1}$, $\tilde{g}$, $\tilde{\boldsymbol{v}}$, t_{k+1}, t_k, t_0, $\boldsymbol{T}^{s}_{imu}$, $\boldsymbol{T}^{s_0}_{s_k}$, $\boldsymbol{r}^{s_0}_{s_k/s_0}$, $\boldsymbol{r}^{s_{k+1}}_{p_{k+1}/s_{k+1}}$):

$\Delta t = t_{k+1} - t_k$

if $\Delta t > 0$ **then**

State Prop($\boldsymbol{r}^{i}_{imu_k}$, $\boldsymbol{v}^{i}_{imu_k}$, $\boldsymbol{T}^{imu_k}_{i}$, $\boldsymbol{b}^{imu}_{accel}$, $\boldsymbol{b}^{imu}_{gyro}$, Δt, $\tilde{g}$, $\boldsymbol{T}^{hdl}_{imu}$, $\boldsymbol{T}^{s_0}_{s_k}$, $\boldsymbol{r}^{s_0}_{s_k/s_0}$)

return $\left(\boldsymbol{r}^{i}_{imu_{k+1}}, \boldsymbol{v}^{i}_{imu_{k+1}}, \boldsymbol{T}^{imu_{k+1}}_{i}, \boldsymbol{T}^{s_0}_{s_{k+1}}, \boldsymbol{r}^{s_0}_{s_{k+1}/s_0}\right)$

else

$\boldsymbol{r}^{i}_{imu_{k+1}} = \boldsymbol{r}^{i}_{imu_k}$

$\boldsymbol{v}^{i}_{imu_{k+1}} = \boldsymbol{v}^{i}_{imu_k}$

$\boldsymbol{T}^{imu_{k+1}}_{i} = \boldsymbol{T}^{imu_k}_{i}$

$\boldsymbol{T}^{s_0}_{s_{k+1}} = \boldsymbol{T}^{s_0}_{s_k}$

$\boldsymbol{r}^{s_0}_{s_{k+1}/s_0} = \boldsymbol{r}^{s_0}_{s_k/s_0}$

$\boldsymbol{r}^{s_0}_{p_0/s_0} = \boldsymbol{r}^{s_0}_{s_{k+1}/s_0} + \boldsymbol{T}^{s_0}_{s_{k+1}} \boldsymbol{r}^{s_{k+1}}_{p_{k+1}/s_{k+1}} - \boldsymbol{T}^{s_0}_{i} \tilde{\boldsymbol{v}} \Delta t$

return $\left(\boldsymbol{r}^{i}_{imu_{k+1}}, \boldsymbol{v}^{i}_{imu_{k+1}}, \boldsymbol{T}^{imu_{k+1}}_{i}, \boldsymbol{T}^{s_0}_{s_{k+1}}, \boldsymbol{r}^{s_0}_{s_{k+1}/s_0}, \boldsymbol{r}^{s_0}_{p_0/s_0}\right)$

State Prop($\boldsymbol{r}^{i}_{imu_k}$, $\boldsymbol{v}^{i}_{imu_k}$, $\boldsymbol{T}^{imu_k}_{i}$, $\boldsymbol{b}^{imu}_{accel}$, $\boldsymbol{b}^{imu}_{gyro}$, Δt, $\tilde{g}$, $\boldsymbol{T}^{s}_{imu}$, $\boldsymbol{T}^{s_0}_{s_k}$, $\boldsymbol{r}^{s_0}_{s_k/s_0}$)

$\Delta \boldsymbol{v}^{imu}_{imu/i} = \left(\left(\dot{\boldsymbol{v}}^{imu}_{imu/i}\right)_m - \boldsymbol{b}^{imu}_{accel}\right) \Delta t$

$\Delta \boldsymbol{\theta}^{imu}_{imu/i} = \left(\left(\dot{\boldsymbol{\theta}}^{imu}_{imu/i}\right)_m - \boldsymbol{b}^{imu}_{gyro}\right) \Delta t$

$\boldsymbol{r}^{i}_{imu_{k+1}} = \boldsymbol{r}^{i}_{imu_k} + \boldsymbol{v}^{i}_{imu_k} \Delta t + \frac{1}{2} \boldsymbol{T}^{i}_{imu_k} \left(\boldsymbol{I}_3 \Delta \boldsymbol{v}^{imu_k}_{imu_{k+1}/i} \Delta t\right) + \frac{1}{2} \left(\boldsymbol{r}^{i}_{imu_k} \tilde{g}\right) \Delta t^2$

$\boldsymbol{v}^{i}_{imu_{k+1}} = \boldsymbol{v}^{i}_{imu_k} + \boldsymbol{T}^{i}_{imu_k} \left(\boldsymbol{I}_3 \Delta \boldsymbol{v}^{imu_k}_{imu_{k+1}/i}\right) + \left(\boldsymbol{r}^{i}_{imu_k} \tilde{g}\right) \Delta t$

$\boldsymbol{T}^{imu_{k+1}}_{i} = \left(\boldsymbol{I}_3 - \left[\Delta \boldsymbol{\theta}^{imu_k}_{imu_{k+1}/i} \times\right]\right) \boldsymbol{T}^{imu_k}_{i}$

$\boldsymbol{T}^{s_0}_{s_{k+1}} = \boldsymbol{T}^{s_0}_{s_k} \left(\boldsymbol{T}^{s}_{imu} \left(\boldsymbol{I}_3 + \left[\Delta \boldsymbol{\theta}^{imu_k}_{imu_{k+1}/i} \times\right]\right) \boldsymbol{T}^{imu}_{s}\right)$

$\boldsymbol{r}^{s_0}_{s_{k+1}/s_0} = \boldsymbol{r}^{s_0}_{s_k/s_0} + \boldsymbol{v}^{i}_{imu_k} \Delta t + \frac{1}{2} \boldsymbol{T}^{i}_{imu_k} \left(\boldsymbol{I}_3 \Delta \boldsymbol{v}^{imu_k}_{imu_{k+1}/i} \Delta t\right) + \frac{1}{2} \left(\boldsymbol{r}^{i}_{imu_k} \tilde{g}\right) \Delta t^2$

return $\left(\boldsymbol{r}^{i}_{imu_{k+1}}, \boldsymbol{v}^{i}_{imu_{k+1}}, \boldsymbol{T}^{imu_{k+1}}_{i}, \boldsymbol{T}^{s_0}_{s_{k+1}}, \boldsymbol{r}^{s_0}_{s_{k+1}/s_0}\right)$

VI. Results

Data from two of the scans performed during helicopter testing are examined to determine the errors incurred by making the preceding approximations in motion compensation. These scans were taken on March 11 (scan A) and March 13 (scan B), 2025. The east-north-up (ENU) position, velocity, and attitude states over the course of the two scans are given in Figures (3)–(4). These states are taken from the GPS-aided navigation filter telemetry, not the motion compensation output.

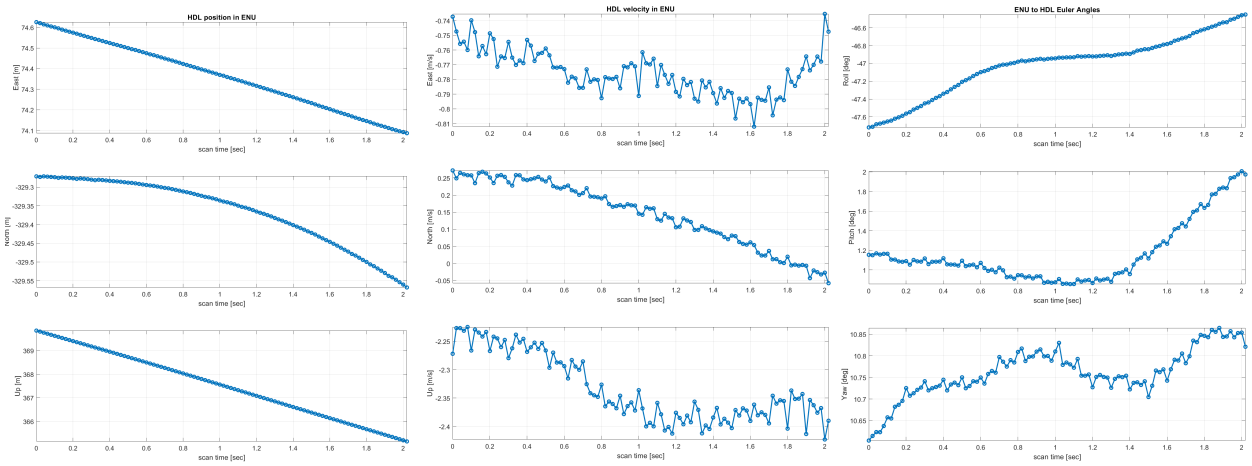

(a) **(b)** **(c)**

Fig. 3 Scan A ENU frame position (a), velocity (b), and attitude (c) from the GPS-aided state solution. ENU frame origin is the DEM origin.

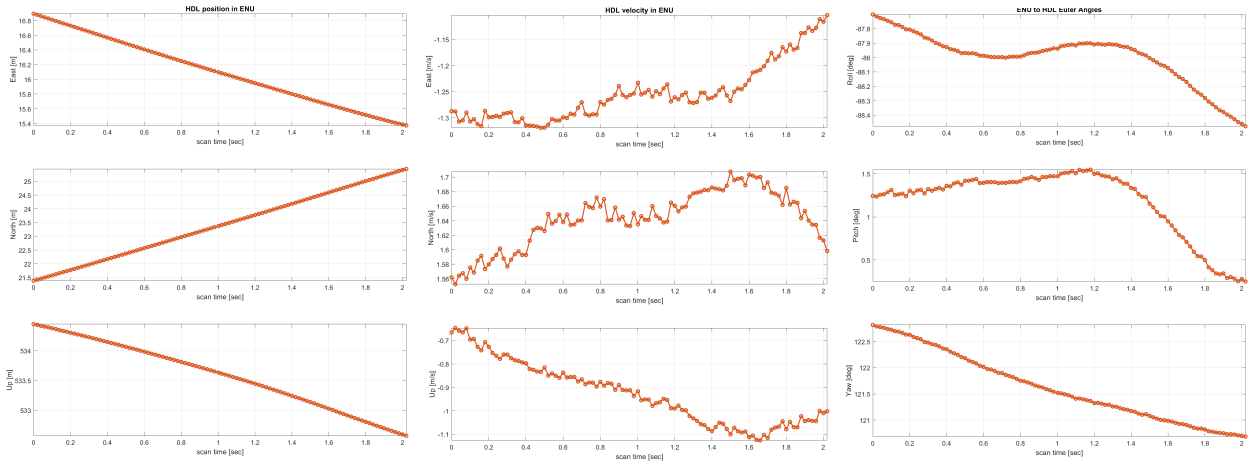

(a) **(b)** **(c)**

Fig. 4 Scan B ENU frame position (a), velocity (b), and attitude (c) from the GPS-aided state solution. ENU frame origin is the DEM origin.

To demonstrate the need for motion compensation, Figure (5) shows the scan A and B resulting point clouds with no motion compensation applied. For the purposes of comparison, a "truth" or baseline point cloud is generated using Eq. (4) and the state propagation equations in Eqs. (9), (10), and (11) without approximations. This point cloud is referred to here as the "full fidelity" or baseline set and depicted for both scans in Figure (6). Note that the baseline is not a survey or ground truth as the purpose of this analysis is only to examine the approximations made in motion compensation. Compared to the baseline result, the raw point cloud for scan A is distorted such that recognizable surface features are not distinguishable, while the scan B cloud shows warping of the features that worsens as the scan

progresses. Both raw point clouds also clearly show an unrealistic slope. Recall, the DEM frame is redefined for each scan, so the location and orientation of features will change between scans A and B. It should also be noted that the scan A point cloud in Figure (5) shows some spurious returns in the top portion of the scan that were corrected with an HDL firmware update for later flights. These spurious returns are omitted in Figure (6) to more clearly show the rest of the point cloud; they have no effect on the motion compensation analysis that follows, as the algorithm is only concerned

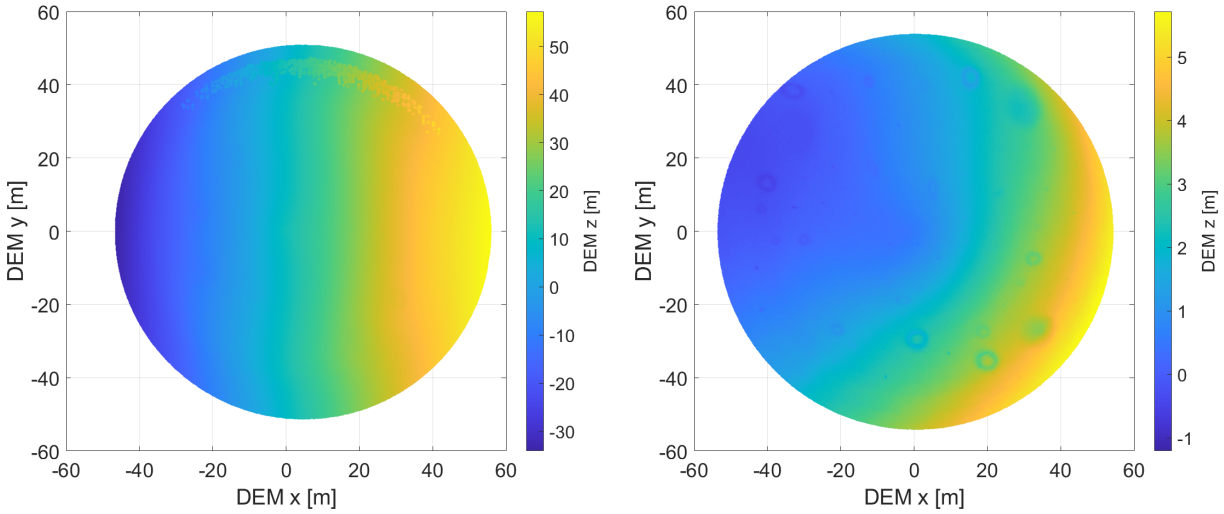

Fig. 5 Point clouds for scan A (a) and B (b) without motion compensation applied.

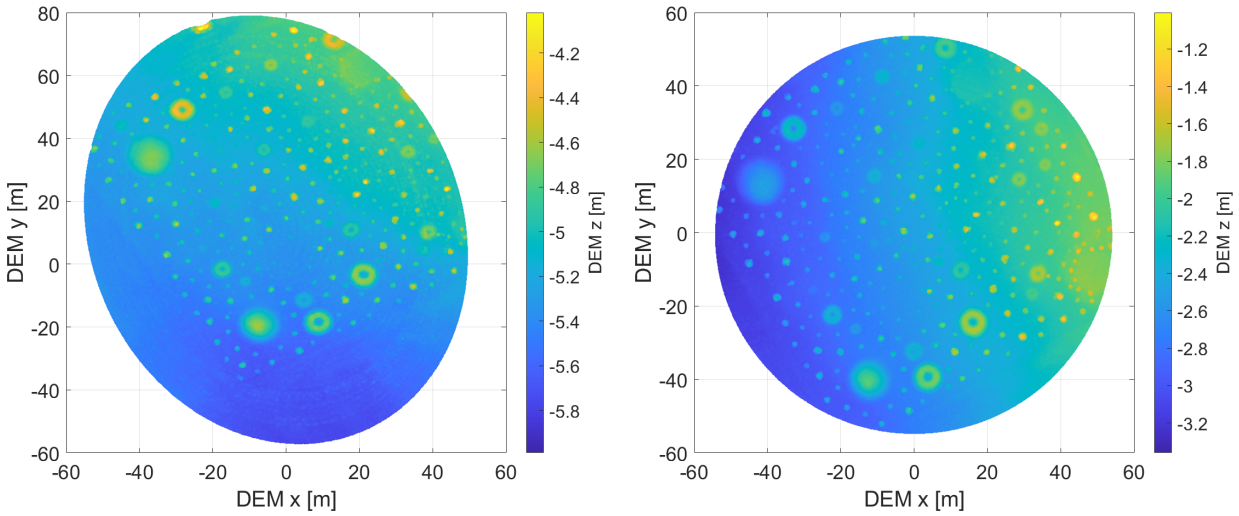

Fig. 6 Point clouds for scan A (a) and B (b) with full fidelity motion compensation applied.

The three primary approximations that are the focus of this analysis are: the gravitational acceleration approximation in Eqs. (17) and (18), neglecting $\Delta\boldsymbol{\theta}^{imu_k}_{imu_{k+1}/i}$ terms in the position and velocity state propagation of Eqs. (9) and (10), and the surface velocity approximation in Eq. (21).

To determine the effect of each approximation of interest on the resulting point cloud, motion compensation is performed on range vector data with each of the approximations applied. The point cloud generated using each approximation is then differenced from the baseline point cloud to determine the error vector for each point.

Error in the point cloud due to the gravitational acceleration approximation is visualized in Figures (7a) and (7b),

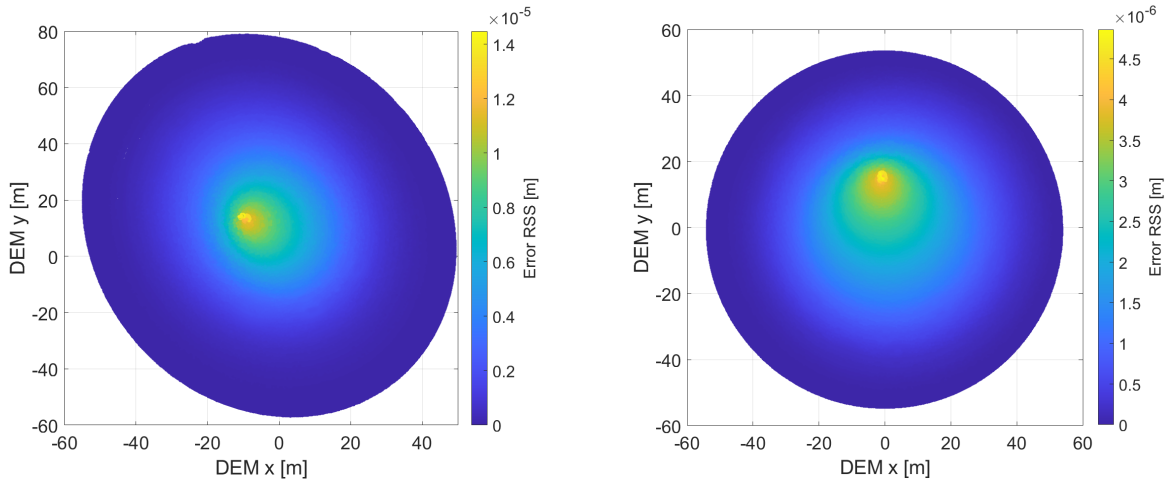

(a) (b)

Fig. 7 Scan A (a) and scan B (b) point clouds using the gravitational acceleration approximation, color coded by error RSS compared to their respective baselines

with the point clouds plotted and color coded by error root-sum-squared (RSS). Error growth follows the scan pattern; as the HDL spirals inward over the course of the scan, the propagation error compounds. A similar trend can be seen in the errors incurred due to decoupling the attitude and translational state propagation, RSS results for that approximation are given by the color bars in Figures (8a) and (8b) with the resulting point clouds. Again, as the scan progresses, moving from the outside of the circular footprint inward, the error RSS for subsequent range vectors increases. Compared to the RSS for a given point in the gravitational acceleration approximation point cloud, the decoupled attitude RSS values are lower. The final analysis of interest is the error incurred via the surface velocity vector approximation. Error RSS results for each range vector are shown in the color coding of Figures (9a) and (9b) for the plotted point clouds. It is clear, the effect of this last approximation results in errors several orders of magnitude larger than the other two approximations combined.

A. Motion Compensation on Other Primary Bodies

The HDL scan, DEM construction, hazard detection, and divert site selection concept of operations is ultimately of interest for EDL on other primary bodies. Specifically, the motion compensation algorithm and associated approximations were designed and selected for a lunar south pole landing. The terrestrial flight test data can be manipulated to get an idea of the magnitude of error incurred by the motion compensation approximations. To produce a synthetic trajectory and IMU data on another primary body instead of Earth, the position and velocity data are transformed from Earth-centered inertial (ECI) to latitude, longitude, altitude (LLA). The attitude data are transformed from IMU with respect to ECI to IMU with respect to ENU. The LLA- and ENU-relative PVA time histories are then taken to be expressed in the LLA and ENU of the new primary body of interest (e.g. Mars).

Using the new primary body constants for semimajor axis and flattening, the PVA data are transformed into position and velocity with respect to the new primary-centered inertial, and IMU orientation with respect to that inertial. With the IMU PVA time history relative to a new pimary-body-centered inertial reference frame, the discrete velocity and attitude propagation equations in Eqs. (10) and (11) are rearranged to solve for the necessary $\Delta\boldsymbol{\nu}^{imu_k}_{imu_{k+1}/i}$ and $\Delta\boldsymbol{\theta}^{imu_k}_{imu_{k+1}/i}$ at each time step. This process is obviously not a perfect kinematic reconstruction of what the terrestrial test would look like on another primary body, but it allows for a coarse examination of the potential errors incurred with this approach to motion compensation.

The same analysis process outlined in Section VI is repeated using Mars, Earth's moon, and Saturn's moon Titan as the primary body. Error growth trends for each approximation are visually similar to those shown in Figures (7), (8), and (9). However, with large differences in rotation rates and gravitational forces of the aforementioned primary bodies compared to Earth, the magnitude of the RSS values for any given point are also significantly different. The maximum RSS values for each primary body, and both scans, are presented in Tables 1 and 2. Also provided in those tables are the Earth-based

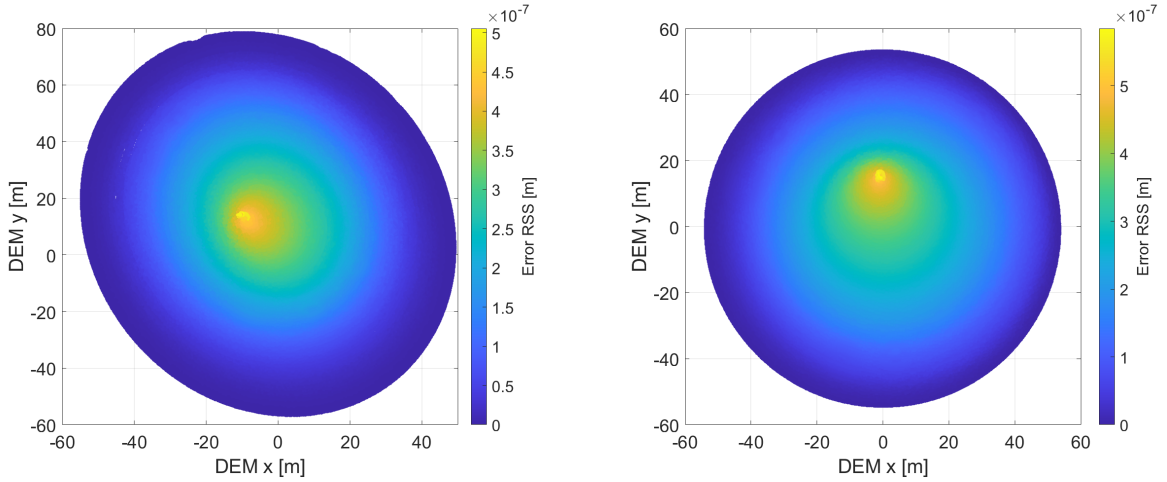

Fig. 8 Scan A (a) and scan B (b) point clouds with attitude decoupled from position and velocity propagation, color coded by error RSS compared to their respective baselines

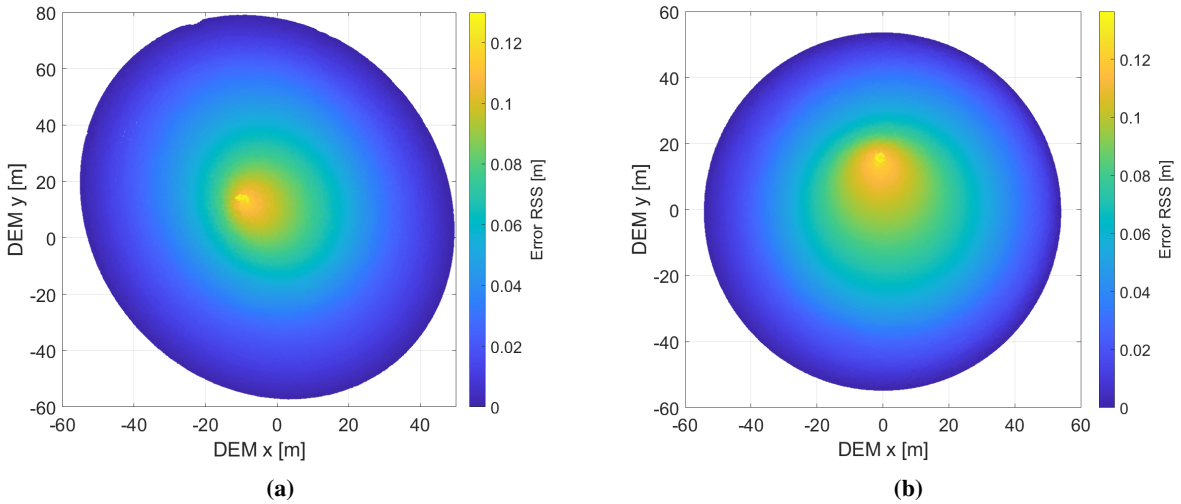

Fig. 9 Scan A (a) and scan B (b) point clouds with the surface velocity approximation, color coded by error RSS compared to their respective baselines

Primary Body	Gravity approx	Decouple attitude	Surface velocity approx.	Combined
Earth	1.44E-5	5.05E-7	0.129	0.129
Earth (synth. IMU)	1.45E-5	5.23E-7	0.129	0.129
Moon	8.64E-6	7.42E-7	2.66E-3	2.66E-3
Mars	1.02E-5	1.88E-7	8,54E-2	8.54E-2
Titan	4.86E-6	5.97E-8	4.55E-3	4.55E-3

Table 1 Scan A, max error RSS in meters of major motion compensation approximations for each primary body. The scan is assumed to occur on the primary body at the same latitude, longitude, and surface-relative altitude as the original terrestrial flight.

Primary Body	Gravity approx	Decouple attitude	Surface velocity approx.	Combined
Earth	4.86E-6	5.84E-7	0.136	0.136
Earth (synth. IMU)	5.51E-6	2.23E-7	0.136	0.136
Moon	3.10E-6	5.25E-8	2.50E-3	2.50E-3
Mars	3.74E-6	9.46E-8	8.85E-2	8.85E-2
Titan	1.74E-6	4.80E-8	4.28E-3	4.28E-3

Table 2 Scan B, max error RSS in meters of major motion compensation approximations for each primary body. The scan is assumed to occur on the primary body at the same latitude, longitude, and surface-relative altitude as the original terrestrial flight.

maximum RSS results and the results for an Earth-based scan using the process outlined above to produce synthetic IMU data from the state time histories. This gives an idea of the relative error incurred by the imperfect process used to regenerate the trajectory, demonstrating it is close enough to examine order of magnitude trends across different primary bodies.

VII. Conclusions

Hazard detection and avoidance is paramount for successful landing operations in hazardous locations or conditions. One approach supported by the SPLICE team has been the maturation of the NASA Goddard HDL. By collecting and processing a spiral scan of the intended landing site, a DEM is produced to detect potential hazards. This paper provides an algorithm for LIDAR motion compensation with simplifications to ensure successful real time operation and DEM creation on an FPGA. Three major simplifications/assumptions are discussed in detail: a gravitational acceleration approximation, decoupling attitude propagation from position and velocity propagation, and a surface velocity vector approximation. The error induced by each simplification is examined using flight test data from March 2025. Results indicate the gravitational acceleration approximation and decoupling of attitude propagation produce negligible errors compared to the surface velocity approximation. Since the motion compensation model was originally developed with a lunar south pole concept of operations in mind, it follows that the error due to this approximation in the lunar case would be significantly smaller at the south pole. For future terrestrial testing and other non-polar applications, this approximation will need to be revised. Additional future work includes sensitivity analysis to the state propagation cadence. That is, determining the error induced by updating the states and motion correction terms at a lower rate than the range returns to potentially free up some computational resources during the scan.

Acknowledgments

HDL flight testing and the derivative analysis presented in this work were made possible by the combined efforts of the SPLICE and HDL teams. The authors wish to thank the teams for their contributions to get to and through flight testing. The authors also wish to thank Dr. Stephen Scheidt from the University of Maryland for his hazard field survey and post-processing contributions.

This work was authored by employees of Draper under Contract No. 80JSC021DA005 with the National Aeronautics and Space Administration. The United States Government retains and the publisher, by accepting the article for publication, acknowledges that the United States Government retains a non-exclusive, paid-up, irrevocable, worldwide

References

[1] Tuttle, M. E., and Bowman, A., "Artemis III Mission Description," , 2025. URL \url{https://www.nasa.gov/mission/artemis-iii/}, accessed: 2025-09-30.

[2] Yim, D., and Bowman, A., "Commercial Lunar Payload Services Description," , 2025. URL \url{https://www.nasa.gov/commercial-lunar-payload-services/}, accessed: 2025-09-30.

[3] Liu, J. Y., Chen, P.-T., Aldrich, J. B., Bocchino, R. L., and Vaughan, G. M., *Current Status and Analyses of the SPLICE Hazard Detection Software*, 2025. https://doi.org/10.2514/6.2025-0928, URL https://arc.aiaa.org/doi/abs/10.2514/6.2025-0928.

[4] Schwartz, R., Mattis, Z., Owens, C., Yothers, M., Khatiwada, B., Venkateswaran, R. K., Morales, N., Porter, R., Sanchez, H. A. L., Mohammadi, M. E., Stephans, T., Beck, D., Jensrud, B., Shaffer, J., Klein, T., Brunecz, D., Begley, A., Shaffer, B., Carey, E., Lindenfelser, H., and Horchler, A. D., "Hazard Detection LiDAR System for Robotic Lunar Landers: Flight Test Results," *AIAA SCITECH 2025 Forum*, 2025. https://doi.org/10.2514/6.2025-1119, URL https://arc.aiaa.org/doi/abs/10.2514/6.2025-1119.

[5] Rutishauser, D., Epp, C., and Robertson, E., "Free-Flight Terrestrial Rocket Lander Demonstration for NASA's Autonomous Landing and Hazard Avoidance Technology (ALHAT) System," *AIAA SPACE 2012 Conference & Exposition*, 2012. https://doi.org/10.2514/6.2012-5239, URL https://arc.aiaa.org/doi/abs/10.2514/6.2012-5239.

[6] Carson, J. M., Munk, M. M., Sostaric, R. R., Estes, J. N., Amzajerdian, F., Blair, J. B., Rutishauser, D. K., Restrepo, C. I., Dwyer-Cianciolo, A. M., Chen, G., and Tse, T., *The SPLICE Project: Continuing NASA Development of GN&C Technologies for Safe and Precise Landing*, 2019. https://doi.org/10.2514/6.2019-0660, URL https://arc.aiaa.org/doi/abs/10.2514/6.2019-0660.

[7] Doll, J. A., Wagner, S. T., Fritz, M., Jang, J.-W., Harper, J. M., Smith, K. W., Acikmese, B., Pedrotty, S. M., and Mendeck, G. F., *Performance Analysis of a Dual Quaternion Guidance Algorithm applicable during Lunar Approach with a Hazard Avoidance Maneuver*, 2024. https://doi.org/10.2514/6.2024-1757, URL https://arc.aiaa.org/doi/abs/10.2514/6.2024-1757.

[8] Ward, K. C., Smith, K. W., Rowe, I. S., Harper, J. M., Adams, D. W., Pedrotty, S. M., and Mendeck, G. F., "Lidar-Based Safe Site Relative Navigation," *AIAA SCITECH 2024 Forum*, 2024. https://doi.org/10.2514/6.2024-1583, URL https://arc.aiaa.org/doi/abs/10.2514/6.2024-1583.

[9] Adams, D. W., Ward, K., and Smith, K. W., "Topographic Slant Range Modeling and Fault Detection for Precision Planetary Landing," *AIAA SCITECH 2025 Forum*, 2025. https://doi.org/10.2514/6.2025-2074, URL https://arc.aiaa.org/doi/abs/10.2514/6.2025-2074.

[10] Restrepo, C. I., Chen, P.-T., Sostaric, R. R., and Carson, J. M., "Next-Generation NASA Hazard Detection System Development," *AIAA Scitech 2020 Forum*, 2020. https://doi.org/10.2514/6.2020-0368.

[11] He, L., Jin, Z., and Gao, Z., "De-Skewing LiDAR Scan for Refinement of Local Mapping," *Sensors*, Vol. 20, No. 7, 2020. https://doi.org/10.3390/s20071846, URL https://www.mdpi.com/1424-8220/20/7/1846.

[12] Chen, P.-T., Liu, J. Y., Bocchino Jr., R. L., Mendeck, G., and Vaughan, G., "Hazard Detection Flight Software for Processing LIDAR Generated DEM," *AIAA Scitech 2026 Forum, to appear*, 2026.